

Role of neutron pairing with density-gradient dependence in the semi-microscopic treatment of the inner crust of neutron stars.

N. Chamel,¹ J. M. Pearson,² and N. N. Shchepochin¹

¹*Institut d'Astronomie et d'Astrophysique, CP-226,
Université Libre de Bruxelles, 1050 Brussels, Belgium*

²*Dépt. de Physique, Université de Montréal, Montréal (Québec), H3C 3J7 Canada*

(Dated: October 18, 2024)

Using the fourth-order extended Thomas-Fermi method with Strutinsky-integral shell and pairing corrections, we calculate the inner crust of neutron stars with the BSk31 functional, whose pairing has two terms: i) a term that is fitted to the results of microscopic calculations on homogeneous nuclear matter (accounting for both medium polarization and self-energy effects) that are more realistic than those of our earlier functionals; ii) an empirical term that is dependent on the density gradient, which permits an excellent fit to nuclear masses. Both proton and neutron pairing are taken into account, the former in the BCS theory and the latter in the local density approximation. We found that the equilibrium value of the proton number Z remains 40 over the entire density range considered, whether or not neutron pairing is included. The new equation of state and the composition are very similar to those of our previously preferred functional, BSk24. However, the predicted neutron pairing fields are quite different. In particular, clusters are found to be impermeable to the neutron superfluid. The implications for the neutron superfluid dynamics are briefly discussed. Since the new pairing is more realistic, the functional BSk31 is better suited for investigating neutron superfluidity in neutron-star crusts.

PACS numbers:

I. INTRODUCTION

Three distinct regions are conventionally recognized in neutron stars (see, for example, Ref. [1] for a recent review). The outermost of these regions, the “outer crust”, consists of a Coulomb crystal of bound nuclei and electrons that globally is electrically neutral. The nuclei in this region become more and more neutron-rich with increasing depth, until at a mean baryon number density \bar{n} of around $2.6 \times 10^{-4} \text{ fm}^{-3}$ unbound neutrons start to appear. This so-called “neutron drip” marks the transition to the “inner crust”, an inhomogeneous assembly of neutron-proton clusters arranged on a crystal lattice and unbound neutrons, with electrons assuring global neutrality. By the point where \bar{n} has risen to about 0.08 fm^{-3} the inhomogeneities have been smoothed out: the “core” of the star has been reached.

In our 2018 paper [2], the inner crust was calculated in the framework of spherical Wigner-Seitz (WS) cells, with both droplet and bubble configurations being admitted. To calculate the energy per nucleon in this framework, we used the ETFSI+pairing (fourth-order extended Thomas-Fermi plus Strutinsky integral with pairing) approach, a high-speed approximation to the Hartree-Fock- Bogoliubov (HFB) method consisting of two distinct stages: a semi-classical extended Thomas-Fermi (ETF) calculation of the total energy, followed by the addition of proton shell corrections, calculated by the Strutinsky-integral method (SI), and proton pairing corrections, handled in the Bardeen-Cooper-Schrieffer (BCS) approximation. For these calculations, we used a family of nuclear energy density functionals that we developed not only for the study of neutron-star structure but also for the general purpose of providing a unified treatment of a wide variety of phenomena associated with the birth and death of neutron stars, such as core-collapse supernovae and neutron-star mergers, along with the r-process of nucleosynthesis (see Ref. [3] and references therein). These functionals are based on generalized Skyrme-type forces and density-dependent contact pairing forces, the parameters of which were determined primarily by fitting to essentially all the nuclear-mass data of the 2012 Atomic Mass Evaluation [4]. In those fits we calculated nuclear masses using the HFB method with axially-symmetric deformation taken into account; the necessary HFB formalism for our generalized Skyrme functionals is given in Refs. [5–7]. Our fits were made subject to certain constraints, the most significant of which was to require consistency, up to the densities prevailing in neutron-star cores, with the equation of state (EoS) of homogeneous pure neutron matter, as calculated *ab initio* from realistic two- and three-nucleon forces. Later, we showed [8–10], that at densities approaching that of the crust-core transition configurations with non-spherical “pasta” shapes became energetically favored. “Spaghetti” and “lasagna” shapes were first predicted by Ravenhall *et al.* [11] and Hashimoto *et al.* [12] some forty years ago, and have subsequently been found in many different approaches. This part of the neutron star is known as the “mantle”. While it is often considered to be an integral part of the inner crust there are good reasons for treating it as a distinct fourth region, since it is expected to behave like liquid crystals [13]. Neither in Ref. [2] nor in any other of our papers on the EoS did we include SI or pairing corrections for neutrons. The omission of the SI correction for neutrons was justified by the argument that neutron shell effects are known to be much smaller

than proton shell effects [14]; in fact, we showed in Section I of Ref. [9] that the situation is a little more complicated, but that the omission of the neutron SI correction is nevertheless expected to be a fairly good approximation. Indeed, a comparison of full 3D band-theory calculations with HF calculations performed in spherical WS cells shows that the neutron shell effects found in the latter are largely spurious: they arise as a result of the discretization imposed by the spherical WS cell approximation on the quasi-continuous spectrum of the unbound single-particle (s.p.) neutron states [15]. Thus in this respect the ETFSI+pairing method may actually be more reliable than HFB calculations performed in spherical WS cells.

On the other hand, we certainly need to take neutron pairing into account if we wish to include neutron superfluidity in the list of phenomena that our functionals can describe. All the functionals used in Ref. [2], BSk22, BSk24, BSk25 and BSk26, contain a neutron-pairing term, and it would have been possible to take account of it in the EoS. As a matter of fact, neutron pairing for BSk22 and BSk24 has recently been included within the ETFSI framework in Refs. [20, 21] in the local-density approximation (LDA). Moreover, 1S_0 pairing gaps and non-dissipative mutual entrainment coefficients of the neutron-proton superfluid mixture in the outer core of a neutron star have been calculated for BSk24 in Ref. [22], varying the temperature and the superflow velocities. However, such calculations are somewhat incomplete for the following reason. The pairing term in the functionals of Ref. [2] is determined analytically at each point in the inhomogeneous nuclear system in question (nucleus in the original HFB fits, WS cell in the inner crust of neutron stars) in such a way as to reproduce the 1S_0 pairing gaps of homogeneous nuclear matter (HNM) of the appropriate density and charge asymmetry, as determined in the *ab initio* calculations made by Cao et al. [23] with realistic two- and three-nucleon forces. These latter gap calculations were made both with and without self-energy corrections [23], but the excellent mass fits found for the functionals of Ref. [2] were obtained by adopting the latter option, since taking account of the self-energy corrections led to gaps that are much smaller, too small to obtain good mass fits. However, while good mass fits are essential for a reliable determination of the composition of the crust, gaps calculated with self-energy corrections are more realistic and thus more appropriate for the reliable study of superfluidity and superconductivity in neutron stars.

It was the realization of this point that led to the construction of a new family of functionals, BSk30–32 [24], functionals that achieve the dual purpose of retaining the excellent mass fits of the earlier functionals while simultaneously being much more suitable for the calculation of superfluidity and superconductivity in neutron stars. They do this by having two pairing terms, the first of which is fitted to the HNM gaps of Ref. [23] calculated *with* the self-energy corrections included, to which is added a phenomenological surface term, i.e., one dependent on the local density gradients, the strength of which is a parameter of the mass fit. The three functionals BSk30–32 were fitted to HNM symmetry coefficients of $J = 30, 31$ and 32 MeV, respectively, and BSk31 gave the best mass fit of the three, with a root mean square (rms) error of 0.571 MeV for 2353 measured masses, as compared with 0.549 MeV for BSk24, our previously preferred functional, whose pairing is less realistic. The overall mass fit of BSk30 is almost as good, but BSk31 does significantly better for neutron-rich nuclei. An examination of the errors of the different functionals suggests that the best fit would have been obtained with a value of J of around 30.6 MeV, midway between the values corresponding to BSk30 and BSk31, and close to the value for BSk24, 30 MeV.

The present paper describes the first EoS calculations made with the functional BSk31, and is the first in which we include neutron pairing. This functional is just as well adapted to a unified treatment of all three regions of neutron stars as the functionals we used in Ref. [2], and we intend to make such calculations in the near future. However, in this paper we confine ourselves to the inner crust, dealing with the special problems posed by the density-gradient dependence of the pairing. Moreover, since our handling of pasta is undergoing further refinement we will limit our calculations in the present paper to densities lower than 0.06 fm^{-3} so that the WS cells can safely be assumed to be spherical; this restriction will be of no consequence for our main concern here, which is to demonstrate the role of neutron pairing, and the changes that it brings about. The fact that the proton pairing is also more realistic with functional BSk31 means that more reliable calculations of proton superconductivity will be possible, but this phenomenon only comes into play at densities higher than 0.06 fm^{-3} , where protons become unbound, and will not be considered here.

Our calculation of the properties of the inner crust with the functional BSk31 are made with our usual ETFSI method. The new feature, neutron pairing, is handled in the LDA; for proton pairing, however, we retain the usual BCS method [25]. Using functionals BSk24 and SLy4, the authors of Ref. [20] find that provided the ETFSI method takes neutron pairing into account it is in good agreement, as far as the energy per nucleon is concerned, with HFB calculations performed in spherical WS cells. The only difference is that these HFB calculations show the optimum value of the number Z of protons in the spherical WS cell to be fluctuating between 36 and 50 as the mean density changes, while there are no such fluctuations with the ETFSI calculations. However, since the energy changes associated with the fluctuations are very small there is no impact on the level of agreement between the two methods. In any case, the fluctuations in Z could be spurious, as explained above. We thus conclude that the ETFSI method used here provides an accurate approximation to the energy per nucleon obtained in the HFB method within the spherical WS cell approximation. Deviations in the optimum values of Z lie within the errors of such implementation

of the HFB method in the range of densities \bar{n} considered here. Moreover, the high speed of the ETFSI approximation is of crucial importance for the large-scale calculations that we are undertaking.

Section II, where we describe our method of calculation, is devoted primarily to our handling of the new pairing, with its dependence on the density gradient, while our results are presented and discussed in Sections III and IV, respectively.

II. METHOD OF CALCULATION

Adopting the ETFSI method, we write the energy per nucleon as

$$e_{\text{ETFSI}} = e_{\text{ETF}} + \frac{1}{A} (E_p^{\text{SI}} + E_p^{\text{pair}} + E_n^{\text{pair}}) \quad , \quad (1)$$

in which e_{ETF} is the energy per nucleon calculated by the ETF method, E_p^{SI} is the SI shell correction for protons in a WS cell with A nucleons and E_q^{pair} is the pairing energy for protons or neutrons, as $q = p$ or n , respectively. The justification for the neglect of the SI correction for neutrons has been discussed above in Section I.

The ETF method consists of expanding the Bloch density matrix in powers of \hbar [42], so that the ETF energy becomes a functional of only the nucleon densities and their gradients. We parametrize the spherically symmetrical density distributions according to

$$\widetilde{n}_q(r) = n_{\text{B}q} + \frac{n_{\Lambda q}}{1 + \exp \left[\left(\frac{C_q - R}{r - R} \right)^2 - 1 \right] \exp \left(\frac{r - C_q}{a_q} \right)} \quad , \quad (2)$$

in which the first term represents a constant background and the second describes the cluster centered around $r = 0$. Here $n_{\Lambda q}$ modulates the density excess due to the cluster, while the geometrical parameters C_q and a_q control the cluster size and the diffuseness of its surface. The first exponential factor in the denominator of the second term of Eq. (2) was introduced [26] in order for the first derivative of the density profile to vanish on the cell surface at $r = R$, a necessary condition established by Wigner and Seitz [27] (note that this condition is not satisfied by the simple Fermi parametrization adopted in Refs. [20, 21]). In fact, with this profile *all* derivatives vanish on the cell surface, which allows us to use an integrated form of the fourth-order ETF method, in which only first- and second-order derivatives of the density appear. It was recently shown that the resulting profile is not suitable for pasta, but is quite acceptable for densities below 0.06 fm^{-3} , to which we limit ourselves here. [28]. For a fixed value of Z , the number of protons per cell, the ETF energy per nucleon is minimized with respect to the geometrical parameters of the neutron and proton distributions (2) and N , the number of neutron per cell (not necessarily an integer, since some neutrons are unbound and thus not confined to one cell).

With the ETF part of the calculation complete, our code then computes the smooth single-particle (s.p.) proton central and spin-orbit fields, $\widetilde{U}_p(r)$ and $\widetilde{\mathbf{W}}_p(r)$, respectively, the Coulomb field $\widetilde{U}_C(r)$ and the effective proton mass $\widetilde{M}_p^*(r)$. The HF equation

$$\left\{ -\nabla \frac{\hbar^2}{2\widetilde{M}_p^*(r)} \cdot \nabla + \widetilde{U}_p(r) + \widetilde{U}_C(r) - i\widetilde{\mathbf{W}}_p(r) \cdot \nabla \times \boldsymbol{\sigma} \right\} \psi_{p,\nu} = \widetilde{\epsilon}_{p,\nu} \psi_{p,\nu} \quad , \quad (3)$$

is then solved with these fixed fields for the s.p. proton energies $\widetilde{\epsilon}_{p,\nu}$, after which proton pairing is calculated with our usual handling of the BCS method, as in Refs. [2, 25]. The proton SI correction appearing in Eq. (1) then becomes (see Appendix A for the proof)

$$E_p^{\text{SI}} = \sum_{\nu} V_{p,\nu}^2 \widetilde{\epsilon}_{p,\nu} - \int d^3\mathbf{r} \left\{ \frac{\hbar^2}{2\widetilde{M}_p^*(r)} \widetilde{\tau}_p(r) + \widetilde{n}_p(r) [\widetilde{U}_p(r) + \widetilde{U}_C(r)] + \widetilde{\mathbf{J}}_p(r) \cdot \widetilde{\mathbf{W}}_p(r) \right\} \quad , \quad (4)$$

in which the $V_{p,\nu}^2$ quantities are the s.p. occupation probabilities, as given, for example, by Eq. (7) of Ref. [25]; the summation goes over all the s.p. proton states. Also $\widetilde{n}_p(r)$, $\widetilde{\tau}_p(r)$ and $\widetilde{\mathbf{J}}_p(r)$ are the smoothed values of the proton density $n_p(r)$, the kinetic proton density $\tau_p(r)$ and the proton spin-current vector density $\mathbf{J}_p(r)$ emerging from the minimization of the ETF energy in the first stage of the calculation; their presence in the second stage of the ETFSI method ensures a high level of self-consistency in the calculation of the shell and pairing corrections.

For the proton pairing energy appearing in Eq. (1) we take the BCS expression

$$E_p^{\text{pair}} = -\frac{1}{4} \sum_{\nu} \frac{\Delta_{p,\nu}^2}{E_{p,\nu}} \quad , \quad (5)$$

where the proton gaps $\Delta_{p,\nu}$ are given by the usual BCS equations, as in Eq. (9b) of Ref. [25], and the proton quasi-particle energies $E_{p,\nu}$ by Eq. (8) of Ref. [25] (see also Appendix A).

The numerical implementation of the BCS method for neutrons is much more challenging since their unbound s.p. states form a quasi-continuum (see, e.g., Ref. [29]), and we adopt rather an LDA. In this way E_n^{pair} becomes a functional of the neutron and proton densities only, and it is thus natural to treat it as being part of the ETF energy and therefore to optimize the ETF energy including the neutron pairing term. If this term were added after minimization, the equilibrium value of N for given Z would remain unchanged. This would certainly be wrong physically and would disagree with exact HFB calculations.

The neutron pairing energy E_n^{pair} is thus determined by adding to the energy density, *before* optimization of the ETF part of the calculation, the quantity [30]

$$\mathcal{E}_{\text{cond},n}(r) = -\frac{3}{8} \widetilde{n}_n(r) \frac{\widetilde{\Delta}_n(r)^2}{\epsilon_{F_n}(r)} \quad , \quad (6)$$

where the neutron pairing field $\widetilde{\Delta}_n(r)$ is defined as the neutron pairing gap obtained locally by solving at each point r in the inhomogeneous matter distribution the same BCS gap equations as in homogeneous nuclear matter with neutron density $\widetilde{n}_n(r)$ and proton density $\widetilde{n}_p(r)$ (see below). Here $\epsilon_{F_n}(r)$ is the local neutron Fermi energy,

$$\epsilon_{F_n}(r) = \frac{\hbar^2 k_{F_n}(r)^2}{2M_n^*(r)} \quad , \quad (7)$$

where

$$k_{F_n}(r) = [3\pi^2 \widetilde{n}_n(r)]^{1/3} \quad . \quad (8)$$

Then

$$E_n^{\text{pair}} = \int d^3\mathbf{r} \mathcal{E}_{\text{cond},n}(r) \quad . \quad (9)$$

The whole process is then repeated for different values of Z in order to achieve optimization with respect to this parameter also. For further details on the ETFSI method, as we have used it in the past, Refs. [2, 25, 26, 31] should be consulted, since we devote the rest of this section to the density-gradient part of the pairing term of the BSk30-32 functionals, which we have to include in the ETFSI formalism for the first time.

Our pairing interaction has the form, for two nucleons of charge type q (n or p) at positions \mathbf{r}_i and \mathbf{r}_j respectively (introducing the relative and center-of-mass coordinates $\mathbf{r}_{ij} = \mathbf{r}_i - \mathbf{r}_j$ and $\mathbf{r} = (\mathbf{r}_i + \mathbf{r}_j)/2$ respectively)

$$v^{\text{pair},q}(\mathbf{r}_i, \mathbf{r}_j) = f_q^{\pm} v^{\pi,q}(\mathbf{r}) \delta(\mathbf{r}_{ij}) \quad , \quad (10)$$

$$v^{\pi,q}(\mathbf{r}) = v^{\text{hom},q}[n_n(\mathbf{r}), n_p(\mathbf{r})] + \kappa_q |\nabla n(\mathbf{r})|^2 \quad , \quad (11)$$

which, with a slight change of notation, is just Eq. (9) of Ref. [24]. The f_q^{\pm} factors here are for fine tuning and are always very close to or exactly equal to unity, while $n = n_n + n_p$. The κ_q term, which was absent in the functionals used in our previous calculations of the inner crust, was introduced to give a better fit to nuclear masses while reproducing exactly the realistic HNM pairing calculations of Cao et al. [23]. In achieving this end, it must be presumed that our surface pairing has been improved.

All our functionals starting from BSk16 [32] and prior to those of Ref. [24] (with the exception of BSk27 [33], which had an older form of pairing) had only the first term of Eq. (11). Aside from the fine-tuning parameters f_q^{\pm} , the pairing in those earlier papers was completely determined *ab initio*, being given at any point \mathbf{r} where the neutron density is $n_n(\mathbf{r})$ and the proton density is $n_p(\mathbf{r})$ by [7]

$$v^{\text{hom},q}[n_n(\mathbf{r}), n_p(\mathbf{r})] = -\frac{8\pi^2}{I_q[n_n(\mathbf{r}), n_p(\mathbf{r})]} \left(\frac{\hbar^2}{2M_q^*[n_n(\mathbf{r}), n_p(\mathbf{r})]} \right)^{3/2} \quad . \quad (12)$$

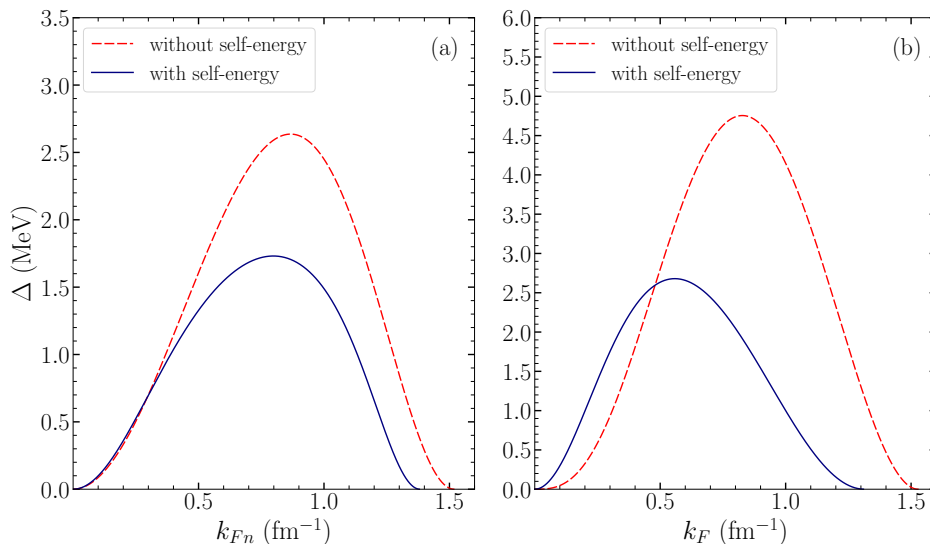


FIG. 1: The 1S_0 pairing gaps of Cao et al. [23] (in MeV) for (a) pure neutron matter and (b) charge-symmetric nuclear matter, shown as a function of the appropriate Fermi wave number (in fm^{-1}) (see text). The results of their calculations with self-energy effects included are denoted by filled symbols, those without by empty symbols. The curves represent our fits to the calculated points. Figure from Ref. [24].

Here $M_q^*[n_n(\mathbf{r}), n_p(\mathbf{r})]$ is the local effective mass for nucleons of charge type q , while

$$I_q[n_n(\mathbf{r}), n_p(\mathbf{r})] = \sqrt{\epsilon_{Fq}(\mathbf{r})} \left[2 \ln \left(\frac{2\epsilon_{Fq}(\mathbf{r})}{\Delta_q(\mathbf{r})} \right) + \Lambda \left(\frac{\epsilon_\Lambda}{\epsilon_{Fq}(\mathbf{r})} \right) \right]. \quad (13)$$

In this last expression $\Delta_q(\mathbf{r}) = \Delta_q[n_n(\mathbf{r}), n_p(\mathbf{r})]$ is the local pairing gap for HNM with neutron density $n_n(\mathbf{r})$ and proton density $n_p(\mathbf{r})$ from the calculations of Cao et al. [23], and $\epsilon_{Fn}(\mathbf{r})$ is the local Fermi energy given by Eq. (7) for neutrons (the expression is similar for protons). It is to be noted that prior to Ref. [24], Eq. (12) and the local Fermi energy entering Eq. (13) were calculated replacing the effective mass by the bare mass for consistency with the absence of self-energy corrections in the adopted HNM gaps of Cao et al. [23] (these gaps were calculated using the free single-particle energy spectrum). Also ϵ_Λ is the cutoff above the Fermi level, while

$$\Lambda(x) = \ln(16x) + 2\sqrt{1+x} - 2 \ln(1 + \sqrt{1+x}) - 4. \quad (14)$$

Equation (12) is nothing but the BCS gap equation in homogeneous nuclear matter with neutron density $n_n(\mathbf{r})$ and proton density $n_p(\mathbf{r})$. Here, it was solved for the pairing interaction $v^{\text{hom},q}[n_n(\mathbf{r}), n_p(\mathbf{r})]$ given the pairing gaps $\Delta_q(\mathbf{r})$.

The pairing force $v^{\text{pair},q}(\mathbf{r}_i, \mathbf{r}_j)$, as given by Eqs. (10) – (13), was used directly in the finite-nucleus HFB calculations of Ref. [24] on which the functional BSk31 was based; the pairing parameters f_q^\pm, κ_q and ϵ_Λ (along with all the Skyrme parameters of BSk31) are given in Table I of Ref. [24]. It is also used in the same way for the BCS calculations of the proton pairing in the present paper. For neutron pairing, which is calculated in the LDA, Eqs. (6)-(9) imply that we need the neutron pairing field $\widetilde{\Delta}_n(r)$ corresponding to the complete pairing term (11). The LDA amounts to locally solving the BCS gap equations for homogeneous nuclear matter with neutron density $\widetilde{n}_n(r)$ and proton density $\widetilde{n}_p(r)$ using the complete pairing interaction with gradient term setting $f_n^\pm = 1$. This can be achieved by simply inverting Eq. (12) using the full pairing interaction (11) instead of $v^{\text{hom},q}$, and this leads to

$$\widetilde{\Delta}_n(r) = 2\epsilon_{Fn}(r) \exp \left[\frac{2\pi^2 \hbar^2}{v_\Lambda^{\text{pair},n}(r) M_n^*[\widetilde{n}_n(r), \widetilde{n}_p(r)] k_{Fn}(r)} \right], \quad (15)$$

in which we have introduced the effective pairing strength

$$v_\Lambda^{\text{pair},q}(r) = \left[\frac{1}{v^{\text{pair},q}(r)} + \frac{M_q^*[\widetilde{n}_n(r), \widetilde{n}_p(r)] k_{Fq}(r)}{4\pi^2 \hbar^2} \Lambda \left(\frac{\epsilon_\Lambda}{\epsilon_{Fq}(r)} \right) \right]^{-1}. \quad (16)$$

With the BSk24 functional adopted in our previous works, there was no density-gradient term in the associated pairing force. If we adopted the same functional here, approximating the effective mass by the bare mass in the

TABLE I: Parameters for Eqns. (18a) and (18b).

	Δ_0 [MeV]	k_1 [fm $^{-1}$]	k_2 [fm $^{-1}$]	k_3 [fm $^{-1}$]	k_m [fm $^{-1}$]
SM	11.5586	0.489932	1.31420	0.906146	1.31
NM	3.37968	0.556092	1.38236	0.327517	1.38

local Fermi energy entering Eq. (13) as discussed above, the neutron pairing field $\widetilde{\Delta}_n(r)$ would reduce to the local pairing gaps $\Delta_n[\widetilde{n}_n(r), \widetilde{n}_p(r)]$, as given by Eq. (17), and we could substitute them directly into Eq. (6), without ever constructing any actual pairing force, as implemented in Refs. [20, 21].

This short-cut is no longer possible now, and having determined the first term on the right-hand side of Eq. (11) from the *ab initio* gaps of Cao et al. [23] we now have to add to it the gradient term to construct the complete pairing force (11) entering Eq. (16). The corresponding neutron pairing field $\widetilde{\Delta}_n(r)$ obtained from Eq. (15) no longer coincides with the local pairing gaps $\Delta_n[\widetilde{n}_n(r), \widetilde{n}_p(r)]$.

Cao et al. [23] only calculated the gaps $\Delta_q(n_n, n_p)$ for pure neutron matter (NM) and charge-symmetric nuclear matter (SM); their results are shown in Fig. 1. For arbitrary asymmetry $\eta \equiv (n_n - n_p)/(n_n + n_p)$ we interpolated [6] according to

$$\Delta_q(n_n, n_p) = \Delta_{\text{SM}}(n)(1 - |\eta|) \pm \Delta_{\text{NM}}(n_q)\eta \frac{n_q}{n} \quad , \quad (17)$$

where we take the upper (lower) sign for $q = n(p)$. Note that this interpolation satisfies the charge symmetry of the nuclear interactions so that the proton pairing gap in pure proton matter at density n is the same as the neutron pairing gap in neutron matter at the same density n , i.e. $\Delta_p(0, n) = \Delta_n(n, 0) = \Delta_{\text{NM}}(n)$. We parametrize the curves $\Delta_{\text{SM}}(n)$ and $\Delta_{\text{NM}}(n)$ of Fig. 1, thus

$$\Delta_{\text{NM}}(n) = \theta(k_m - k_{Fn})\Delta_0 \frac{k_{Fn}^2}{k_{Fn}^2 + k_1^2} \frac{(k_{Fn} - k_2)^2}{(k_{Fn} - k_2)^2 + k_3^2} \quad (18a)$$

and

$$\Delta_{\text{SM}}(n) = \theta(k_m - k_F)\Delta_0 \frac{k_F^2}{k_F^2 + k_1^2} \frac{(k_F - k_2)^2}{(k_F - k_2)^2 + k_3^2} \quad . \quad (18b)$$

Here $k_F = (3\pi^2 n/2)^{1/3}$, $k_{Fn} = (3\pi^2 n_n)^{1/3}$, θ is the unit-step Heaviside function and the parameters Δ_0, k_1, k_2, k_3 and k_m are given in Table I. Note that this parametrization is valid only for the gaps that Cao et al. [23] calculated with self-energy corrections (filled symbols in Fig. 1); it is the gap parametrization that was adopted in Ref. [24] (but not shown there) for the construction of functionals BSk30, BSk31 and BSk32, and is therefore the one adopted here. The parametrization of the gaps that Cao et al. [23] calculated without self-energy corrections, and which we adopted for our earlier functionals, in particular for BSk24, will be found in Ref. [6].

III. RESULTS

Assuming spherical WS cells, we have performed calculations with the new functional BSk31 over the inner crust from its interface with the outer crust, i.e., from the neutron drip point, up to a mean local density \bar{n} of 6.0×10^{-2} fm $^{-3}$, beyond which point proton drip and pasta formation could not have been excluded.

A. Energy and pressure

In Fig. 2 we show for BSk31 the energy per nucleon e as a function of the mean density \bar{n} . The same figure also shows results for our previously preferred functional, BSk24, calculated with no neutron pairing, as in all our earlier calculations with this functional. No significant difference between the two functionals will be seen, but the fact that the BSk31 rises more steeply at high densities suggests that its EoS will be stiffer, i.e., the pressure will rise more rapidly with density. This is confirmed in Fig. 3. Note that the pressure calculated with BSk31 now includes the correction due to pairing (see Appendix B).

It would be unsafe to assume that these small differences are a result of neutron pairing being included in BSk31 but not in BSk24, since the two functionals were fitted to different values of the symmetry coefficient J . Accordingly, to

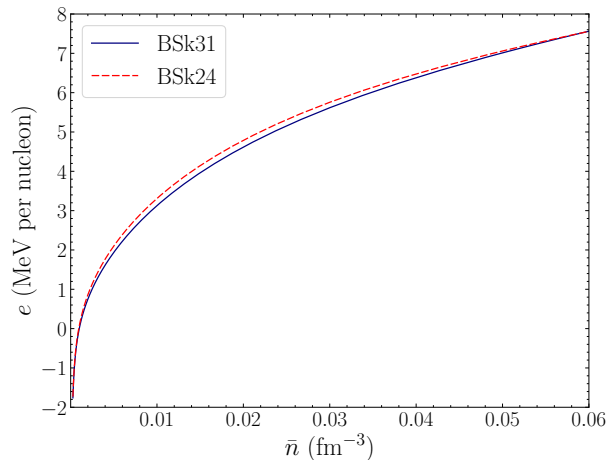


FIG. 2: Energy per nucleon (in MeV) in the inner crust of a neutron star as function of mean density \bar{n} (in fm^{-3}) for functionals BSk31 and BSk24.

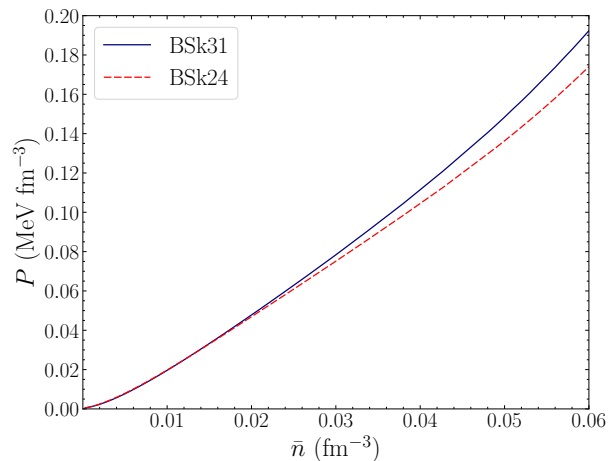


FIG. 3: Pressure (in MeV fm^{-3}) in the inner crust of a neutron star as function of mean density \bar{n} (in fm^{-3}) for functionals BSk31 and BSk24.

assess the impact of neutron pairing on the EoS we repeat the calculations of the last two figures for functional BSk31 without neutron pairing, denoting it by BSk31(-n). If we replot Figs. 2 and 3 with BSk24 replaced by BSk31(-n) the curves for BSk31 and BSk31(-n) would lie very close to each other. Indeed, as can be seen in Fig. 4, neutron pairing contributes only a small fraction of the total energy per nucleon, and leads to a gain in energy of about 0.1 MeV per nucleon at most. At all densities the contribution of neutron pairing to the pressure does not exceed 3%, as shown in Fig. 5. Therefore the changes in the EoS of the inner crust with BSk31 compared with BSk24 are mainly caused by the different symmetry energy.

B. Composition

In Figs. 6, 7 and 8 we show for functionals BSk31 and BSk31(-n) the variation of the energy per nucleon as a function of proton number Z at three different densities spanning the full range considered here. We see that the optimal value of the proton number Z is 40 everywhere, whether or not neutron pairing is included; the same optimal value of Z for functional BSk24 was found in Ref. [2]. However, the energy differences between the different values of Z are so small that considerable mixtures of different values of Z could subsist after the crystallization of the crust [34, 35], with pronounced peaks at $Z = 40$ at all densities. Weaker peaks at $Z = 20$ and 58 will also be found for high densities, and at 28 and 50 for lower densities. It is noteworthy that the magic numbers 20, 40 and 58 all correspond to the closure of ℓ -shells rather than j -shells, pointing to the diminished role of spin-orbit splitting in the greater homogeneity found at higher densities.

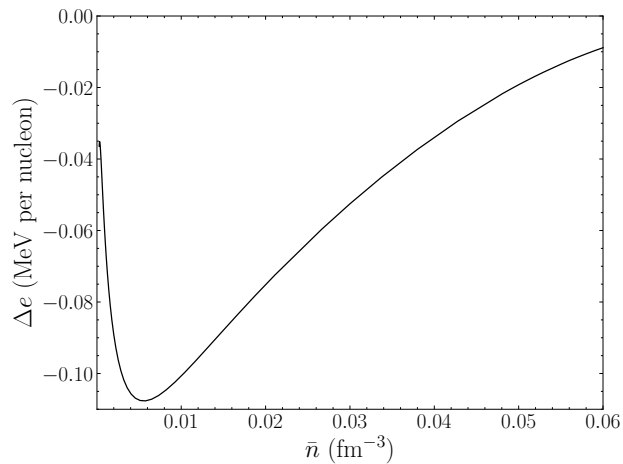


FIG. 4: Difference in energy per nucleon (in MeV) for BSk31 calculated with and without neutron pairing, as function of mean density \bar{n} (in fm^{-3}).

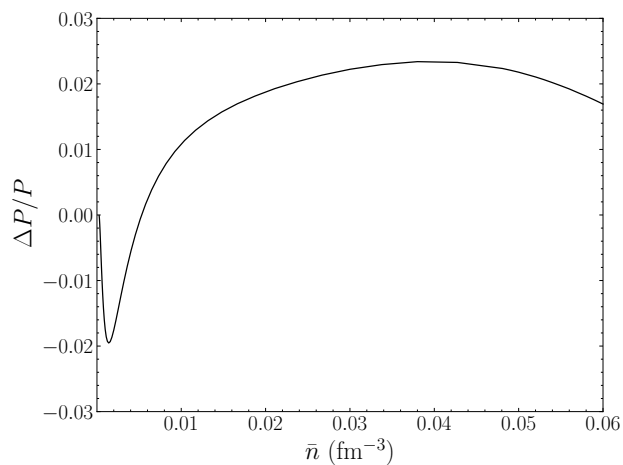


FIG. 5: Relative difference in pressure (in MeV fm^{-3}) for BSk31 calculated with and without neutron pairing as function of mean density \bar{n} (in fm^{-3}).

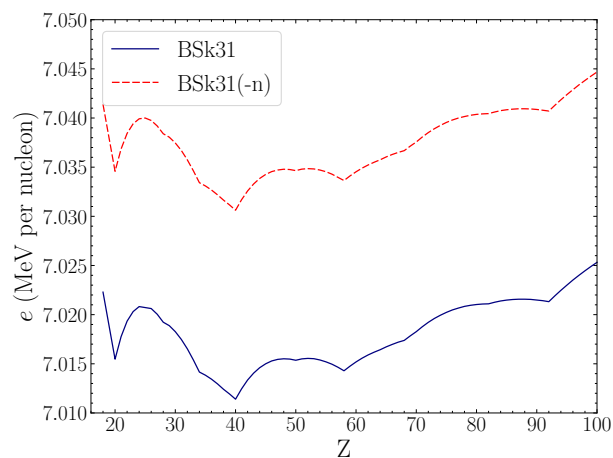


FIG. 6: Energy per nucleon (in MeV) as a function of proton number Z at density \bar{n} of $5.0 \times 10^{-2} \text{ fm}^{-3}$

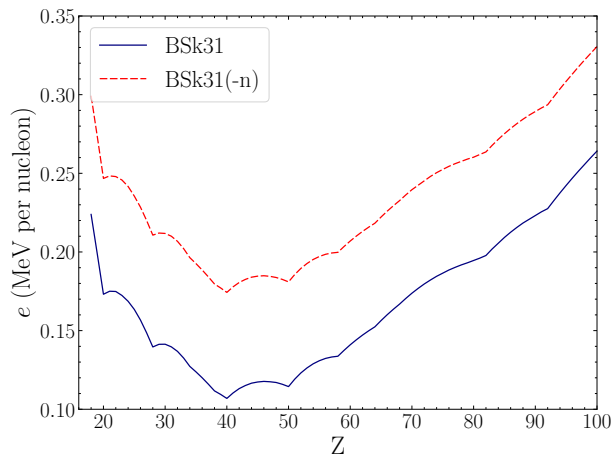


FIG. 7: As for Fig. 6 at density \bar{n} of $1.10967 \times 10^{-3} \text{ fm}^{-3}$

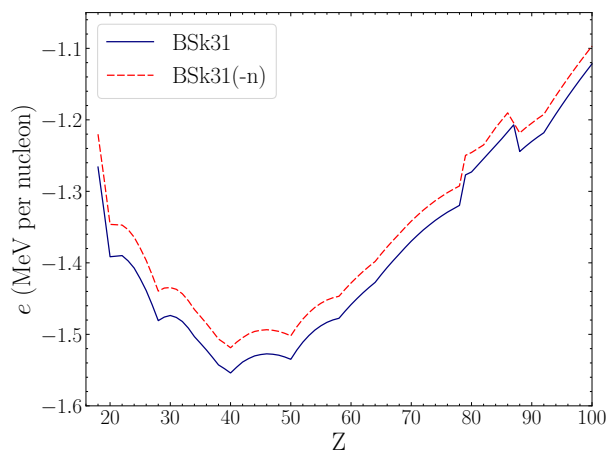


FIG. 8: As for Fig. 6 at density \bar{n} of $3.0375 \times 10^{-4} \text{ fm}^{-3}$

This insensitivity of the composition of the inner crust to the presence or absence of neutron pairing that we find in our ETFSI calculations stands in contrast to what was found in the calculations of Refs. [16–18]. The fluctuations in the optimal value of Z found in the HFB calculations could originate in the spurious shell effects arising from the spherical WS cell approximation [15]. The associated errors propagate throughout the self-consistent calculations and cannot be completely removed [16, 36].

Having established that for functional BSk31 the optimum number Z of protons in the spherical WS cell is 40 over the entire density range considered here, whether or not neutron pairing is included, the question arises as to the optimum number N of neutrons in the cell, and to what extent this depends on the inclusion of neutron pairing. At the same time we note that the optimum value of N will depend also on the value of the symmetry coefficient J of HNM for the functional in question. We thus compare BSk31 not only with BSk31(-n) but also with BSk30, for which $J = 30 \text{ MeV}$; the latter, like BSk31, will be calculated with and without the inclusion of neutron pairing. A complication arises from the fact that for BSk30 the optimum value of Z in the inner crust is equal to 40 only up to $\bar{n} \approx 0.002 \text{ fm}^{-3}$; for higher densities the preferred value of Z is 58, although the energetic advantage is very slight. We thus study not the optimum value of N but rather that of the proton fraction $Y_p = Z/(N + Z)$.

The optimum values of Y_p are shown as a function of mean density in Fig. 9. It will be seen that the role of neutron pairing is negligible compared to that of the symmetry coefficient: the lower value of J is associated with a higher value of Y_p , i.e., fewer neutrons for a given value of Z . This is because at the sub-nuclear densities prevailing in the inner crust the symmetry energy obtained with the BSk30-32 functionals is *greater* for the lower value of J , as can be seen in Fig. 10. It would appear that the symmetry coefficient J to which the functional in question is fitted has a greater impact on the number of neutrons in the spherical WS cell than does neutron pairing. (The kink in both BSk30 curves in the vicinity of $\bar{n} = 0.002 \text{ fm}^{-3}$ is due to the equilibrium value of Z switching from 40 to 58.)

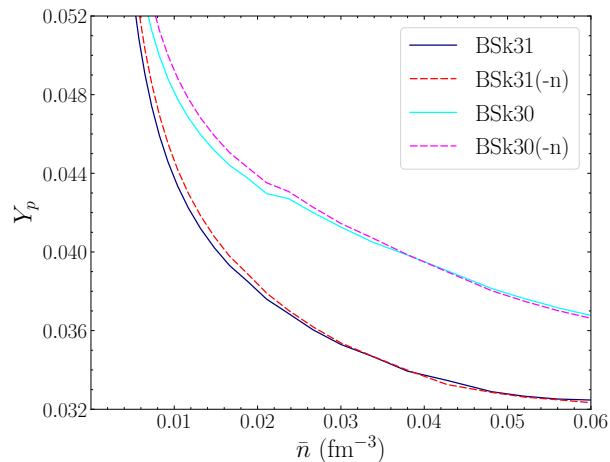


FIG. 9: Proton fraction Y_p in the inner crust of a neutron star as function of mean density (in fm^{-3}).

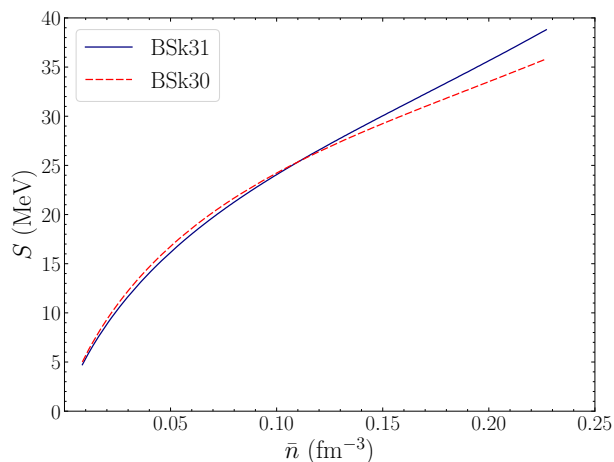


FIG. 10: Symmetry energies (in MeV) of BSk31 and BSk30 as a function of density (in fm^{-3}).

C. Neutron pairing field

In Figs. 11, 12 and 13 we compare the nucleon density distributions $\tilde{n}_q(r)$ and neutron pairing fields $\tilde{\Delta}_n(r)$ generated by the functional BSk31 and those generated by BSk24 with its neutron pairing taken into account, a feature that we indicate by denoting it as BSk24(n). All three figures show the variation of the nucleon density distributions and neutron pairing fields with the radial position r , Fig. 11 for the low mean density of $\bar{n} = 3.0 \times 10^{-4} \text{ fm}^{-3}$, Fig. 12 for the intermediate mean density of $4.0 \times 10^{-3} \text{ fm}^{-3}$ and Fig. 13 for the high mean density of $5.0 \times 10^{-2} \text{ fm}^{-3}$. In all three figures, the curves labelled “BSk31($\kappa = 0$)” relate to calculations performed with functional BSk31 in which the part of the neutron pairing term that depends on the density gradient has been removed. To make the comparisons more meaningful the pairing fields are calculated with the same number of neutrons, $N = 108$ for Fig. 11, 653 for Fig. 12 and 1182 for Fig. 13, these being optimal values for BSk31; in all cases we take $Z = 40$, this being optimal for both functionals at all densities.

At the very low mean density \bar{n} of Fig. 11, close to the interface with the outer crust, we see the strong contribution made by the density-gradient pairing term in BSk31 in the vicinity of $r = 6 \text{ fm}$, which is just the highly inhomogeneous region corresponding to the tail of the cluster term of the density distribution (2). Remarkably, the maximum value of the neutron pairing field turns out to be comparable to that obtained with BSk24(n). To achieve an equally good nuclear mass fit, the absence of a gradient term in the latter could only be compensated by neglecting self-energy effects.

Outside of this region, both close to the center of the cell and towards the surface of the cell, the density distribution is relatively homogeneous and the BSk31 neutron pairing field is determined almost entirely by the reference gap of Cao et al. [23], see Fig. 1. The BSk24(n) neutron pairing field does not exactly coincide with the reference gap of

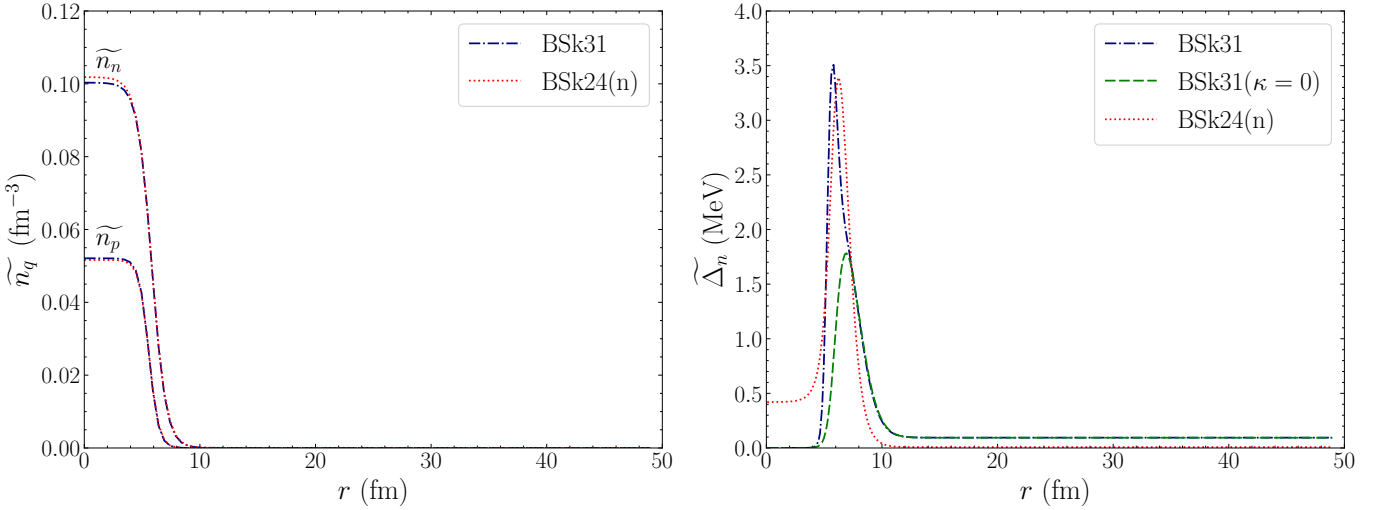


FIG. 11: (left panel) Nucleon density distributions in the inner crust of a neutron star at mean density $\bar{n} = 3.0 \times 10^{-4} \text{ fm}^{-3}$ ($Z = 40$, $A = 148$) as functions of radial position r (in fm) in the spherical WS cell for BSk31 functional (blue dash-dotted lines) and BSk24(n) functional with neutron pairing included (red dotted lines). (Right panel) BSk31 (blue dash-dotted lines) and BSk24(n) (red dotted lines) neutron pairing fields (in MeV) in the spherical WS cell. The pairing field for BSk31 without density gradient term is plotted for comparison (BSk31($\kappa = 0$) - green dashed line).

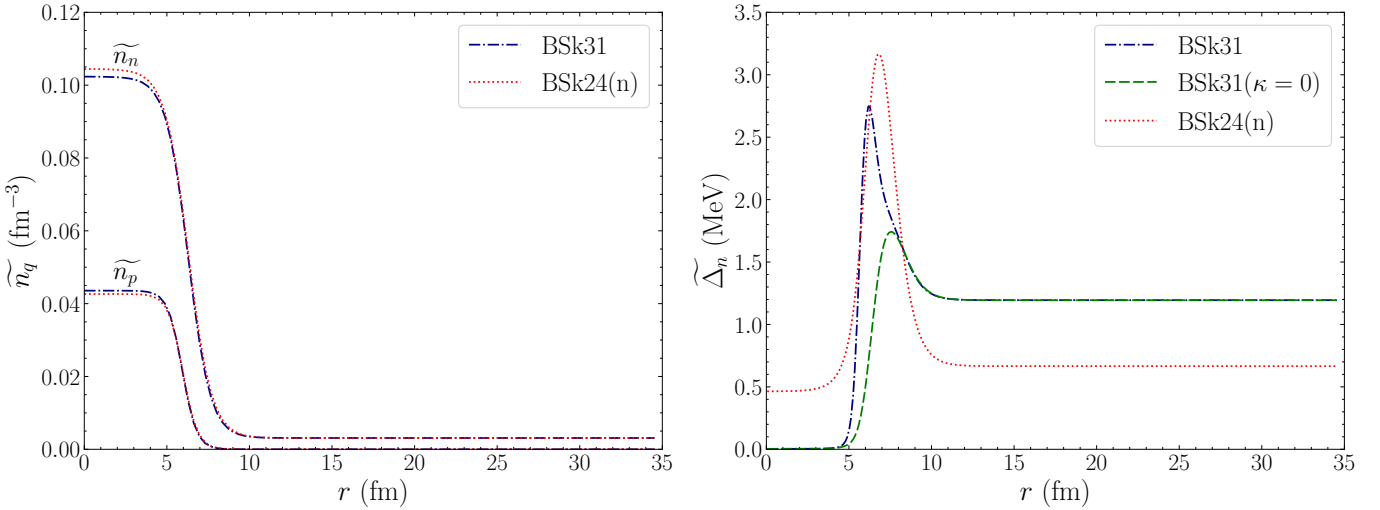


FIG. 12: As for Fig. 11 at density $\bar{n} = 4.0 \times 10^{-3} \text{ fm}^{-3}$ ($Z = 40$, $A = 693$).

Cao et al. [23] because of the substitution of the bare mass instead of the effective mass in the pairing force $v^{\text{pair},q}(\mathbf{r})$ (as well as in the Fermi energy entering the pairing force) but not in Eqs. (15) and (16). At the center of the cluster, $k_F \approx 1.3 \text{ fm}^{-1}$ and $k_{F_n} \approx 1.4 \text{ fm}^{-1}$ correspond to negligibly small SM and NM gaps but only when self-energy effects are included. This explains why the neutron pairing field vanishes for BSk31 while it remains non-negligible for BSk24(n). At the border of the cell, the matter consists mainly of free neutrons and the left panel of Fig. 1 is highly relevant. There, $k_{F_n} \approx 0.1 \text{ fm}^{-1}$ and for this wave number the pairing gaps Δ_{NM} are almost equal for BSk31 and BSk24(n), as can be seen in the left panel of Fig. 1. The differences in the neutron pairing field come from the different treatments of the effective mass in the pairing force.

The situation depicted at the intermediate value of \bar{n} in Fig. 12 is qualitatively unchanged, but at the much higher mean densities \bar{n} close to the mantle the spherical WS cell is everywhere more homogeneous and the density-gradient term in BSk31 is now almost ineffective, as can be seen in Fig. 13 comparing the blue dash-dotted and green dashed curves. Thus the calculated neutron pairing field everywhere strongly resembles the HNM reference gaps. In particular, the strong increase of the neutron pairing field outside clusters stems from the fact that the value of $k_{F_n} \approx 1.0 \text{ fm}^{-1}$ corresponds to the peak of Δ_{NM} shown in the left panel of Fig. 1.

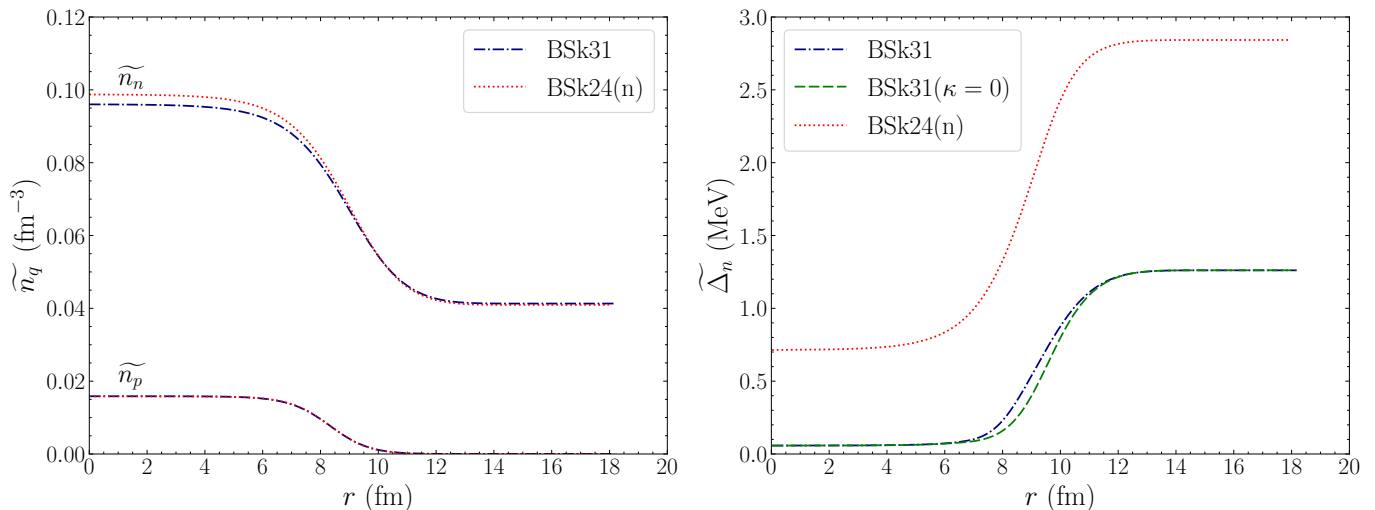


FIG. 13: As for Fig. 11 at density $\bar{n} = 5.0 \times 10^{-2} \text{ fm}^{-3}$ ($Z = 40$, $A = 1222$).

It is apparent from Figs. 11, 12 and 13 that it is only at higher mean densities \bar{n} that the BSk24(n) neutron pairing, which is based on the HNM pairing calculated without self-energy corrections, can be said to be stronger than the BSk31 neutron pairing, but these of course are the densities relevant to the nuclear mass fits.

It is worth noting that Figs. 11, 12 and 13 show that for all values of the mean density \bar{n} the neutron pairing fields remain constant for some distance below the cell surface. This is because the cluster term in (2) becomes vanishingly small for relatively small values of r , beyond which the pairing fields are determined by the background parameters n_{Bn} and n_{Bp} .

IV. CONCLUSION

In this paper, we have further improved our ETFSI treatment of the inner crust of a neutron star by adding neutron pairing within the LDA, using the functional BSk31 [24]. Since the pairing term of this functional depends on the density gradient a fairly extensive modification of our previous treatment is necessary.

Pending the completion of our improved treatment of pasta, our present calculations are confined to densities below 0.06 fm^{-3} where clusters are expected to be quasispherical. We have found that neutron pairing has a marginal impact on the composition. The equilibrium proton number Z remains equal to 40, and the number of neutrons in the spherical WS cell is only slightly altered, a conclusion that is at variance with results obtained from HFB and HF+BCS calculations [16–18]. The conclusions of those calculations, however, are rendered questionable by spurious shell effects arising from the spherical WS cell approximation [15]. Comparing results obtained with BSk30 and BSk31 from the same family but fitted to different values of J shows that the symmetry energy plays a more important role for the composition than does pairing. As expected, the neutron pairing correction to the energy per nucleon is small, being of order 0.1 MeV at most. Likewise, the correction to the pressure does not exceed 3%.

We have shown that while the functional BSk31 is equivalent in many respects to our previously preferred functional BSk24 [3], it has, as expected, quite different neutron-pairing properties. Being more realistically based by including not only medium polarization but also self-energy effects, BSk31 is more suitable for the study of neutron superfluidity in the inner crust of neutron stars. In particular, our calculations suggest that the neutron superfluid dynamics could be qualitatively different, which could have important implications for the global dynamics of neutron stars and the interpretation of astrophysical phenomena, such as pulsar frequency glitches [37]. The key point is the conclusion that while with the functional BSk24(n) the neutron pairing field penetrates the clusters everywhere in the inner crust, with BSk31 the pairing field vanishes inside clusters in all regions of the inner crust but the deepest (see Figs. 12-13). This suggests that the neutron superfluid can flow through the clusters for the functional BSk24(n), but not for the functional BSk31, except close to the interface with the core of the star. To analyze the implication that the neutron superfluid must flow around the clusters in the case of the functional BSk31 one must go beyond the ETFSI+pairing approach adopted here and work within the framework of the time-dependent HFB approach. However, a considerable economy in the computer time consumed by such calculations could be achieved by using the WS-cell parameters (composition and nucleonic distributions) determined in the calculations of the present paper.

Since proton superconductivity only occurs at densities higher than those considered here a comparable study of the proton-pairing properties and proton superconductivity of the functional BSk31 is postponed to a later paper.

Acknowledgments

The work of N.N.S. was financially supported by the FWO (Belgium) and the Fonds de la Recherche Scientifique (Belgium) under the Excellence of Science (EOS) programme (project No. 40007501). This work also received funding from the Fonds de la Recherche Scientifique (Belgium) under Grant No. PDR T.004320 and IISN 4.4502.19.

Appendix A: Generalized Strutinsky-integral theorem

The aim of this appendix is to provide for the first time a rigorous derivation for the SI correction with BCS pairing (4) originally introduced in Ref. [38] in the context of finite nuclei using heuristic arguments. To this end, we generalize the proof of the SI theorem given in Appendix C of Ref. [26] within the pure Hartree-Fock (HF) approach, without pairing.

In the HFB method (see, e.g., Ref. [39]), the energy E_{HFB} of the (normalized) ground-state $|\Psi\rangle$ is expressed as a function of the so-called normal and abnormal density matrices, defined by (we drop here the nucleon label q)

$$n_{ij} = \langle \Psi | c_j^\dagger c_i | \Psi \rangle = \sum_k V_{ik}^* V_{jk} = n_{ji}^* \quad (\text{A1a})$$

and

$$\kappa_{ij} = \langle \Psi | c_j c_i | \Psi \rangle = \sum_k V_{ik}^* U_{jk} = -\kappa_{ji} \quad , \quad (\text{A1b})$$

respectively, with $c_i^\dagger (c_j)$ denoting creation (destruction) operators for nucleons in such states. Here we are working in a fixed basis of discrete s.p. states labelled by i, j , etc., e.g., an oscillator basis (the isospin charge type is implicit in the label). The matrices U_{ij} and V_{ij} can be obtained from the HFB equations

$$\sum_j \begin{pmatrix} h_{ij} - \lambda \delta_{ij} & \Delta_{ij} \\ -\Delta_{ij}^* & -h_{ij}^* + \lambda \delta_{ij} \end{pmatrix} \begin{pmatrix} U_{jk} \\ V_{jk} \end{pmatrix} = E_k \begin{pmatrix} U_{ik} \\ V_{ik} \end{pmatrix} \quad , \quad (\text{A2})$$

where E_k are the quasi-particle energies, λ is the chemical potential, h_{ij} are the matrix elements of the self-consistent s.p. Hamiltonian

$$h_{ij} = \frac{\partial E_{\text{HFB}}}{\partial n_{ji}} = h_{ji}^* \quad , \quad (\text{A3a})$$

and Δ_{ij} are the matrix elements of the pairing potential

$$\Delta_{ij} = \frac{\partial E_{\text{HFB}}}{\partial \kappa_{ij}^*} = -\Delta_{ji} \quad . \quad (\text{A3b})$$

For zero-range density-dependent effective interactions, such as those considered here, the HFB energy is given by

$$E_{\text{HFB}} = \text{Tr} \left(t n + \frac{1}{2} \Gamma n - \frac{1}{2} \Delta \kappa^* \right) \quad , \quad (\text{A4})$$

in which Tr denotes the trace, t_{ij} are the matrix elements of the kinetic-energy operator $-\hbar^2 \nabla^2 / 2M$ (M denoting the nucleon mass), while

$$\Gamma_{kl} = \sum_{ij} \bar{v}_{ki,lj}^{\text{Sky}} n_{ji} + \sum_{ij} \bar{v}_{ki,lj}^{\text{Coul}} n_{ji} \quad , \quad (\text{A5a})$$

and

$$\Delta_{kl} = \frac{1}{2} \sum_{ij} \bar{v}_{kl,ij}^{\text{pair}} \kappa_{ij} \quad , \quad (\text{A5b})$$

where $\bar{v}_{ki,lj}^{\text{Sky}}$, $\bar{v}_{ki,lj}^{\text{Coul}}$ and $\bar{v}_{ki,lj}^{\text{pair}}$ are the antisymmetrized matrix elements of the Skyrme, Coulomb and pairing interactions respectively. Using Eq. (A3a), the matrix elements of the self-consistent s.p. Hamiltonian are thus given by

$$h_{ij} = t_{ij} + \Gamma_{ij} + h_{ij}^{\text{rear}}, \quad (\text{A6})$$

where we have introduced matrix elements of the rearrangement s.p. field

$$h_{ij}^{\text{rear}} \equiv \frac{1}{2} \sum_{klpm} \left(\frac{\partial \bar{v}_{kl,pm}^{\text{Sky}}}{\partial n_{ji}} n_{ml} n_{pk} - \frac{1}{2} \frac{\partial \bar{v}_{kl,pm}^{\text{pair}}}{\partial n_{ji}} \kappa_{pm} \kappa_{ik}^* \right) . \quad (\text{A7})$$

For the relation between this matrix formulation of the HFB equations and the coordinate space formulation, see, e.g., Appendix A of Ref. [32].

Multiplying the second row of Eq. (A2) by V_{ik}^* using Eqs. (A1a), (A1b) and (A6), and summing over k and i yields

$$\text{Tr} (\Delta^* \kappa - t n - \Gamma n - h^{\text{rear}} n) = \sum_{ki} (E_k - \lambda) |V_{ik}|^2 . \quad (\text{A8})$$

Inserting this expression into Eq. (A4) leads to

$$E_{\text{HFB}} = \sum_{ki} (\lambda - E_k) |V_{ik}|^2 - E_{\text{pair}} - \frac{1}{2} \text{Tr} (\Gamma n) - \text{Tr} (h^{\text{rear}} n) , \quad (\text{A9})$$

with the pairing energy

$$E_{\text{pair}} = -(1/2) \text{Tr} (\Delta^* \kappa) \leq 0 . \quad (\text{A10})$$

In the BCS approximation, the matrix elements of the pairing potential are supposed to take the form

$$\Delta_{kl} = \delta_{\bar{k}l} \Delta_{k\bar{k}} , \quad (\text{A11})$$

\bar{k} denoting the time-reversed of the state k in the basis for which the s.p. Hamiltonian is diagonal,

$$h_{ij} = \epsilon_i \delta_{ij} . \quad (\text{A12})$$

Solving now the HFB equations (A2) with this ansatz and making use of the anticommutation and unitarity relations between the U and V matrices (see, for example, Eqs. (7.5) of Ref [39]), we find

$$E_k = \sqrt{(\epsilon_k - \lambda)^2 + \Delta_k^2} , \quad (\text{A13a})$$

$$U_{kk} = U_{\bar{k}\bar{k}} = \frac{1}{\sqrt{2}} \left(1 + \frac{\epsilon_k - \lambda}{E_k} \right)^{1/2} , \quad (\text{A13b})$$

and

$$V_{k\bar{k}} = -V_{\bar{k}k} = \frac{1}{\sqrt{2}} \text{sign}(\Delta_{\bar{k}k}) \left(1 - \frac{\epsilon_k - \lambda}{E_k} \right)^{1/2} \equiv V_k , \quad (\text{A13c})$$

where we have introduced the pairing gaps $\Delta_k \equiv |\Delta_{\bar{k}k}|$ and we have adopted the usual phase convention. Substituting Eqs. (A13b) and (A13c) into Eqs. (A1a) and (A1b) leads to the familiar expressions for the normal and abnormal density matrices,

$$n_{kl} = (V_{k\bar{k}})^2 \delta_{kl} , \quad \kappa_{kl} = V_{k\bar{k}} U_{kk} \delta_{\bar{k}l} . \quad (\text{A14})$$

Using Eqs. (A14) and (A5b) leads to the BCS gap equations

$$\Delta_k = -\frac{1}{4} \sum_l \bar{v}_{kk,ll}^{\text{pair}} \frac{\Delta_l}{E_l} . \quad (\text{A15})$$

The pairing energy, as given by Eq. (A10), reduces to Eq. (5).

In the absence of pairing (HF limit), $\kappa_{ij} = 0$, and therefore $\Delta_{ij} = 0$ in any basis, in particular in the basis of the s.p. Hamiltonian where $h_{ij} = \tilde{\epsilon}_i \delta_{ij}$. Note that $\tilde{\epsilon}_i$ does not generally coincide with ϵ_i because the effective pairing force contributes to the s.p. mean field via rearrangement terms, see Eq. (A7). In the following, we will denote a quantity Q obtained in the HF approximation by \check{Q} . Using Eq. (A13c) yields $\check{V}_i^2 = 1$ if $\tilde{\epsilon}_i \leq \check{\lambda}$ and 0 otherwise. Likewise, Eq. (A13a) leads to $\check{E}_i = |\tilde{\epsilon}_i - \check{\lambda}|$. Using Eq. (A9), we find for the HF ground-state energy

$$E_{\text{HF}} = \sum_i n_i \check{\epsilon}_i - \frac{1}{2} \text{Tr} \left(\check{\Gamma} \check{n} \right) - \text{Tr} \left(\check{h}^{\text{rear}} \check{n} \right) , \quad (\text{A16})$$

where $n_i \equiv \check{V}_i^2$ is the Fermi-Dirac distribution. We shall neglect the (small) differences between the HF and HF+BCS density matrices, i.e. $\check{n}_{ij} \approx n_{ij}$ (hence also $\check{\Gamma}_{ij} \approx \Gamma_{ij}$), as well as the differences in the rearrangement s.p. field, i.e. $\check{h}_{ij}^{\text{rear}} \approx h_{ij}^{\text{rear}}$ therefore $\check{\epsilon}_i \approx \epsilon_i$. With $\check{\lambda} \approx \lambda$, the HF+BCS ground state energy can finally be expressed as

$$E_{\text{HF+BCS}} \approx E_{\text{HF}} - E_{\text{pair}} + \sum_i V_i^2 (\lambda - E_i) - \sum_i n_i \epsilon_i . \quad (\text{A17})$$

On the other hand, the HF energy can be obtained from the Strutinsky-integral theorem (see, e.g., Appendix C of Ref. [26])

$$E_{\text{HF}} \approx E_{\text{ETF}} + \delta E_{\text{HF}} , \quad (\text{A18})$$

where E_{ETF} is the ‘‘macroscopic’’ energy, as calculated using the ETF method [40, 41], and δE_{HF} , given by

$$\delta E_{\text{HF}} = \sum_k n_k \tilde{\epsilon}_k - \int d^3 \mathbf{r} \left(\frac{\hbar^2}{2M^*} \tilde{\tau} + \tilde{n} \tilde{U} + \tilde{\mathbf{J}} \cdot \tilde{\mathbf{W}} \right) , \quad (\text{A19})$$

accounts for shell corrections. Inserting Eq. (A18) in Eq. (A17) using Eq. (A19), we find

$$E_{\text{HF+BCS}} \approx E_{\text{ETF}} + \delta E_{\text{HF+BCS}} , \quad (\text{A20})$$

with

$$\delta E_{\text{HF+BCS}} = \sum_k V_k^2 (\lambda - E_k) - \int d^3 \mathbf{r} \left(\frac{\hbar^2}{2M^*} \tilde{\tau} + \tilde{n} \tilde{U} + \tilde{\mathbf{J}} \cdot \tilde{\mathbf{W}} \right) + \sum_k \frac{\Delta_k^2}{4E_k} . \quad (\text{A21})$$

Using Eqs. (A13a) and (A13c), this expression can be written in the equivalent form

$$\delta E_{\text{HF+BCS}} = \sum_k V_k^2 \epsilon_k - \int d^3 \mathbf{r} \left(\frac{\hbar^2}{2M^*} \tilde{\tau} + \tilde{n} \tilde{U} + \tilde{\mathbf{J}} \cdot \tilde{\mathbf{W}} \right) - \sum_k \frac{\Delta_k^2}{4E_k} , \quad (\text{A22})$$

which is the correction given by Eqs. (4) and (5).

Appendix B: Pairing correction to the pressure

As shown in Ref. [31], the pressure of any crustal layer is the same as that obtained in an homogeneous mixture of neutrons, protons, and electrons with densities n_{Bn} , n_{Bp} , and n_e respectively. For the inner crust region considered here, protons remain bound inside clusters therefore $n_{\text{Bp}} \approx 0$. Therefore, the proton pairing correction to the pressure given by Eq.(B25) of Ref. [31] can be safely neglected. The neutron pairing correction can be calculated from the condensation energy density of pure neutron matter at density n_{Bn} , as

$$\delta P = n_{\text{Bn}}^2 \frac{d(\mathcal{E}_{\text{cond},n}/n_{\text{Bn}})}{dn_{\text{Bn}}} , \quad (\text{B1})$$

where

$$\mathcal{E}_{\text{cond},n} = -\frac{3}{8} n_{\text{Bn}} \frac{\Delta_{\text{NM}}(n_{\text{Bn}})^2}{\epsilon_{\text{Fn}}} , \quad (\text{B2})$$

$$\epsilon_{Fn} = \frac{\hbar^2}{2M_n^*(n_{Bn})} (3\pi^2 n_{Bn})^{2/3}. \quad (\text{B3})$$

The pressure correction for the generalized Skyrme functionals adopted in this work [24] can be expressed as

$$\delta P = \frac{n_{Bn}^{1/3} \Delta_{NM}(n_{Bn}) [3n_{Bn} \Delta_{NM}(n_{Bn}) B_n'(n_{Bn}) + 2B_n(n_{Bn}) (\Delta_{NM}(n_{Bn}) - 3n_{Bn} \Delta'_{NM}(n_{Bn}))]}{8(3\pi^2)^{2/3} B_n(n_{Bn})^2}, \quad (\text{B4})$$

where we have introduced

$$B_n(n_{Bn}) \equiv \frac{\hbar^2}{2M_n^*(n_{Bn})} = \frac{\hbar^2}{2M_n} + \frac{1}{8} \left[t_1(1-x_1) + 3t_2(1+x_2) + t_4(1-x_4)n_{Bn}^\beta + 3t_5(1+x_5)n_{Bn}^\gamma \right] n_{Bn}. \quad (\text{B5})$$

The derivative of $B_n(n_{Bn})$ and $\Delta_{NM}(n_{Bn})$ with respect to n_{Bn} , indicated by a prime, can be easily calculated analytically from the expression above and Eq. (18a) (with $k_{Fn} = (3\pi^2 n_{Bn})^{1/3}$) respectively, and are not explicitly given.

-
- [1] D. Blaschke and N. Chamel, in *The Physics and Astrophysics of Neutron Stars*, edited by L. Rezzolla, P. Pizzochero, D. Jones, N. Rea, and I. Vidaña, Astrophysics and Space Science Library Vol. 457 (Springer, Berlin, 2018), pp. 337–400.
 - [2] J. M. Pearson, N. Chamel, A. Y. Potekhin, A. F. Fantina, C. Ducoin, A. K. Dutta, and S. Goriely, *MNRAS*, **481**, 2944 (2018) [Erratum: *MNRAS*, **486**, 768 (2019)].
 - [3] S. Goriely, N. Chamel, and J. M. Pearson, *Phys. Rev. C* **88**, 024308 (2013).
 - [4] G. Audi, M. Wang, A. H. Wapstra, F. G. Kondev, M. MacCormick, X. Xu, and B. Pfeiffer, *Chinese Physics C* **36**, 1287 (2012).
 - [5] N. Chamel, S. Goriely, and J. M. Pearson, *Phys. Rev. C* **80**, 065804 (2009).
 - [6] S. Goriely, N. Chamel, and J. M. Pearson, *Eur. Phys. Journ. A* **42**, 547 (2009).
 - [7] N. Chamel, *Phys. Rev. C* **82**, 014313 (2010).
 - [8] J. M. Pearson, N. Chamel, and A. Y. Potekhin, *Phys. Rev. C* **101**, 015802 (2020).
 - [9] J. M. Pearson and N. Chamel, *Phys. Rev. C* **105**, 015803 (2022).
 - [10] N. N. Shchepochin, N. Chamel and J. M. Pearson, *Phys. Rev. C* **108**, 025805 (2023).
 - [11] D. G. Ravenhall, C. J. Pethick, and J. R. Wilson, *Phys. Rev. Lett.* **50**, 2066 (1983).
 - [12] M. Hashimoto, H. Seki, and M. Yamada, *Prog. Theor. Phys.* **71**, 320 (1984).
 - [13] A. Y. Potekhin and C. J. Pethick, *Phys. Lett.* **B427**, 7 (1998).
 - [14] K. Oyamatsu and M. Yamada, *Nucl. Phys.* **A578**, 181 (1994).
 - [15] N. Chamel, S. Naimi, E. Khan, and J. Margueron, *Phys. Rev. C* **75**, 055806 (2007).
 - [16] F. Grill, J. Margueron, and N. Sandulescu, *Phys. Rev. C* **84**, 065801 (2011).
 - [17] M. Baldo, U. Lombardo, E.E. Saperstein, S.V. Tolokonnikov, *Nucl. Phys.* **A 750**, 409 (2005).
 - [18] M. Baldo, E.E. Saperstein, S.V. Tolokonnikov, *Phys. Rev. C* **76**, 025803 (2007).
 - [19] M. Baldo, E.E. Saperstein, S.V. Tolokonnikov, *Nucl. Phys.* **A 775**, 235 (2006).
 - [20] M. Shelley and A. Pastore, *Universe* **6**, 206 (2020).
 - [21] M. Shelley and A. Pastore, *Phys. Rev. C* **103**, 035807 (2021).
 - [22] V. Allard and N. Chamel, *Universe* **7** (12), 470 (2021).
 - [23] L.G. Cao, U. Lombardo, and P. Schuck, *Phys. Rev. C* **74**, 064301 (2006).
 - [24] S. Goriely, N. Chamel, and J. M. Pearson, *Phys. Rev. C* **93**, 034337 (2016).
 - [25] J. M. Pearson, N. Chamel, A. Pastore, and S. Goriely, *Phys. Rev. C* **91**, 018801 (2015).
 - [26] M. Onsi, A. K. Dutta, H. Chatri, S. Goriely, N. Chamel, and J. M. Pearson, *Phys. Rev. C* **77**, 065805 (2008).
 - [27] E. Wigner and F. Seitz, *Phys. Rev.* **43**, 804 (1933).
 - [28] N. N. Shchepochin, N. Chamel, J. M. Pearson, A. I. Chugunov, and A. Y. Potekhin, *Phys. Rev. C* **109**, 055802 (2024).
 - [29] N. Chamel, S. Goriely, J. M. Pearson, and M. Onsi, *Phys. Rev. C* **81**, 045804 (2010).
 - [30] P. M. Pizzochero, L. Viverit, and R. A. Brogna, *Phys. Rev. Lett.* **79**, 3347 (1997).
 - [31] J. M. Pearson, N. Chamel, S. Goriely, and C. Ducoin, *Phys. Rev. C* **85**, 065803 (2012).
 - [32] N. Chamel, S. Goriely, J. M. Pearson, *Nucl. Phys.* **A 812**, 72 (2008).
 - [33] S. Goriely, N. Chamel, J. M. Pearson, *Phys. Rev. C* **88**, 061302(R) (2013).
 - [34] T. Carreau, F. Gulminelli, N. Chamel, A. F. Fantina, J. M. Pearson, *A&A* **635**, A84 (2020).
 - [35] T. Carreau, A. F. Fantina, F. Gulminelli, *A&A* **640**, A77 (2020).
 - [36] A. Pastore, M. Shelley, S. Baroni and C. A. Diget, *J. Phys. G* **44**, 094003 (2017).
 - [37] S. Zhou, E. Güğercinoğlu, J. Yuan, M. Ge, C. Yu, *Universe* **8**, 641 (2022).
 - [38] J. M. Pearson, Y. Aboussir, A. K. Dutta, R. C. Nayak, M. Farine, and F. Tondeur, *Nucl. Phys.* **A 528**, 1 (1991).
 - [39] P. Ring, P. Schuck, *The Nuclear Many-Body Problem*, Springer, New York, 1980.
 - [40] J. Bartel, M. Brack, and M. Durand, *Nucl. Phys.* **A445**, 263 (1985).

- [41] M. Onsi, H. Przysiezniak and J. M. Pearson, Phys. Rev. C **55**, 3139 (1997).
- [42] M. Brack, C. Guet, and H. B. Håkansson Phys. Rev. C **123**, 275 (1985).